LiVPO4F1–yOy tavorite-type compositions: influence of the vanadyl-type defects concentration on the structure and electrochemical performance

Edouard Boivin, Rénald David, Jean-Noël Chotard, Tahya Bamine, Antonella Iadecola, Lydie Bourgeois, Emmanuelle Suard, François Fauth, Dany Carlier, Christian Masquelier, et al.

$LiVPO_4F_{1-y}O_y$ Tavorite-type compositions: Influence of the vanadyl-type defects' concentration on the structure and electrochemical performance

Edouard Boivin [a,b,g], Rénald David [b,g], Jean-Noël Chotard [b,g,h], Tahya Bamine [a,g], Antonella Iadecola [g], Lydie Bourgeois [c,d], Emmanuelle Suard [e], François Fauth [f], Dany Carlier [a,g], Christian Masquelier [b,g,h] and Laurence Croguennec [a,g,h,1]

[a] CNRS, Univ. Bordeaux, Bordeaux INP, ICMCB UMR 5026, F-33600 Pessac, France.

[b] Laboratoire de Réactivité et de Chimie des Solides, CNRS UMR 7314, Université de Picardie Jules Verne, F-80039 Amiens Cedex 1, France.

[c] Université de Bordeaux, ISM, Groupe de Spectroscopie Moléculaire, F-33405 Talence, France.

[d] Bordeaux INP, ISM, CNRS UMR 5255, F-33405, Talence, France.

[e] Institut Laue-Langevin, 71 Avenue des Martyrs, F-38000 Grenoble, France.

[f] CELLS - ALBA synchrotron, E-08290 Cerdanyola del Vallès, Barcelona, Spain.

[g] RS2E, Réseau Français sur le Stockage Electrochimique de l'Energie, FR CNRS 3459, F-80039 Amiens Cedex 1, France.

[h] ALISTORE-ERI European Research Institute, FR CNRS 3104, F-80039 Amiens Cedex 1, France.

[1] Corresponding author : L. Croguennec (Laurence.Croguennec@icmcb.cnrs.fr)

Abstract

Mixed valence $LiVPO_4F_{1-y}O_y$ materials were obtained for the first time over a large composition range (here, $0.35 \leq y \leq 0.75$), through a single step solid state synthesis. Interestingly, the competition between the ionic character of the V^{3+}-F bond and the strong covalency of the V^{4+}=O vanadyl bond originates a complex crystal chemistry at the local scale, which allows to stabilize a solid solution between $LiVPO_4F$ and $LiVPO_4O$ despite a significant deviation from the Vegard's law for the cell parameters. A combined study using IR, Raman and X-ray absorption spectroscopies highlights the role of vanadyl environments on the electronic structure of vanadium's orbitals and *a fortiori* the electrochemical behavior. Our results underline that the electrochemical performance of $LiVPO_4F_{1-y}O_y$-type materials can be controlled by tuning the concentration of vanadyl-type defects, i.e. by playing on the competition between the ionic V^{3+}-F and the covalent V^{4+}=O bond.

Introduction

Tavorite compositions, $LiMXO_4Y$, are positive electrode materials of interest for Lithium-ion batteries. Indeed, the working potential of these phases can be adjusted by changing the nature of the transition metal (with M = V, Fe, Mn, Ti), of the polyanionic group (XO_4 with X = P or S) or of the bridging anion (with Y = O, F, OH, H_2O).[1] Therefore, the stabilization of new compositions is a major issue, at both the practical and fundamental level. Vanadium based Tavorite materials $LiVPO_4F$ and $LiVPO_4O$ are the most attractive ones due to their high working voltage (*i.e.* 4.26 and 3.95 V vs Li^+/Li respectively) and thus to their high theoretical energy density[2], strongly competitive with the already commercialized $LiFePO_4$ (655Wh/kg *vs.* Li of theoretical energy density for $LiVPO_4F$ against 586Wh/kg *vs.* Li for $LiFePO_4$).[3] Nevertheless, among the numerous studies which report on apparently pure $LiVPO_4F$, some discrepancies in the average structure and electrochemical properties are observed. Indeed, unit cell volumes fluctuate between V/Z = 87.00 $Å^3$ and V/Z = 87.31 $Å^3$ whereas the difference between $LiVPO_4O$ (V/Z = 85.51 $Å^3$) and $LiVPO_4F$ is around 1.7 $Å^3$. [2,4,5] Recently, Kang and coworkers reported the $LiVPO_4F_{\sim 0.25}O_{\sim 0.75}$ composition whose average structure is similar to the one of $LiVPO_4F$ (despite the large O^{2-}/F^- substitution ratio) and whose electrochemical properties are drastically different.[6] Therefore, the partial substitution of fluorine by oxygen associated with the partial oxidation of V^{3+} to V^{4+}=O (or $\{V=O\}^{2+}$) for charge compensation (*i.e.* the formation of vanadyl-type defects) could be at the origin of these discrepancies. This hypothesis has already been investigated by Nuclear Magnetic Resonance (NMR) spectroscopy and Density Functional Theory (DFT) calculations[7,8] but its experimental validation was still challenging due to the low concentration of defects in $LiVPO_4F$. Therefore, we synthetized $LiVPO_4F_{1-y}O_y$ compositions controlling the substitution ratio of oxygen for fluorine, in order to study the influence of vanadyl-type defects on the average structure as well as on the local environments around vanadium. The electrochemical study performed at high and low voltage domains reveals a strong influence of the vanadyl-type defects' concentration on the electrochemical performance in terms of energy density, cyclability and rate capability.

1. Experimental part

All along this study the $LiV^{III,IV}PO_4F_{1-y}O_y$ compounds will be compared to the end-member phases ($LiV^{III}PO_4F$ and $LiV^{IV}PO_4O$) whose the syntheses are different to that used to prepare the mixed valence phases (given in details in the synthesis part). The quasi stoichiometric $LiVPO_4F$ was synthesized according to the reaction (1), through a two steps carbothermal reduction, as described previously[2]. V_2O_5 (Sigma-Aldrich, > 98%) is reduced by a small excess of C_{SP} carbon (*i.e.* a highly divided soot) in the presence of $NH_4H_2PO_4$ (Sigma-Aldrich, > 99%). A thermal treatment at 800°C under argon flow leads to the formation of VPO_4/C, in which the vanadium phosphate particles are surrounded by residual carbon nanoparticles localized in the grain boundaries. After the addition of a stoichiometric amount of LiF to VPO_4/C, the mixture is annealed at 800°C under argon flow to form $LiVPO_4F$. $LiVPO_4O$ was also synthetized by a solid state reaction from V_2O_3 (Cerac, ≤ 99.9%), Li_3PO_4 (Sigma-Aldrich, 97%) and $NH_4H_2PO_4$ (Sigma-Aldrich, > 99%) as described in reference [2], according to the reaction (2).

(1) Step 1 $V^{V}_2O_5 + 2\ NH_4H_2PO_4 + 2C + C_{excess} \rightarrow 2\ V^{III}PO_4/C + 2\ NH_3 + 2\ CO + 3\ H_2O$

Step 2 $V^{III}PO_4/C + LiF \rightarrow LiV^{III}PO_4F/C$

(2) $V^{III}_2O_3 + 4/3\ NH_4H_2PO_4 + 2/3\ Li_3PO_4 + ½\ O_2 \rightarrow 2\ LiV^{IV}PO_4O + 4/3\ NH_3 + 2\ H_2O$

Scanning Electron Microscopy (SEM) analysis of the samples' morphology was performed using a Hitachi S-4500 microscope. The samples were previously metallized by gold deposition.

In order to confirm the chemical compositions of the samples, the Li, V, and P contents were determined using an Inductively Coupled Plasma / Optical Emission Spectrometry (ICP-OES) spectrometer (Varian 720-ES Optical Emission Spectrometer) after complete dissolution of the powders into a mixture of hydrochloric and nitric acid solutions.

Thermogravimetric analysis coupled with mass spectrometry (TGA-MS) experiments was done on a STA449C Jupiter thermo-microbalance coupled with a QMS Aëolos 32 spectrometer commercialized by Netzsch. The thermal treatments were conducted under air and over a temperature range between 20 and 600°C, with a continuous heating rate of 5°C/min for the first experiment, measuring the concentration of HF (m/z= 20) and CO_2 (m/z=

44) released during the experiments. In order to separate the different weight losses (associated to the release of carbon and fluorine) and overpass the kinetics phenomena, a second experiment was performed, with several plateaus during 1h at the characteristic temperatures identified by the first experiment (*i.e.* 500 and 600°C).

The average oxidation states of vanadium cations were obtained from the measurement of samples' magnetization as function of temperature in the paramagnetic domain using a Vibrating Sample Magnetometer (VSM). A 10000 Oe magnetic field was applied and the temperature was increased from 100K to 500K at a heating rate of 10K/min. The sample holder was a sealed aluminum capsule in which the powder was immobilized with glass fibers' plug. The measured magnetic susceptibility was corrected, according to equation (3), from the contribution of the sample holder (aluminum and glass fiber) and from the diamagnetic contribution of $LiVPO_4(F,O)$ calculated taking into account the diamagnetic susceptibility values of the constituting ions taken from reference [9]:

(3) $(\chi_{para}(LiVPO_4F_{1-y}O_y) = \chi_{mes} - \chi_{dia}(LiVPO_4F_{1-y}O_y) - \chi_{blank})$.

High angular resolution Synchrotron X-ray powder diffraction (SXRPD) experiments were performed at the MSPD beamline of the ALBA synchrotron[10] (Barcelona, Spain). Data were collected using the MYTHEN position sensitive detector in Debye-Scherrer geometry, using a wavelength of 0.9539 Å, over a 2° - 72° angular range (0.006° per step) and a total integration time of 5 minutes. The samples were sealed in a 0.5 mm diameter capillary. Neutron diffraction (ND) was performed at the Institut Laue Langevin (ILL, Grenoble, France) on the high-resolution diffractometer D2B. The samples were contained in an 8 mm diameter vanadium tube, and the diffraction patterns were collected in transmission mode at room temperature, with a wavelength of 1.5950 Å in the 2θ angular range of [0 - 150°] using a 0.05° (2θ) step with a global accumulation time of 12 h. It was necessary to correct the absorption in order to take into account a decrease of the experimental diffracted intensity compared to the expected one. The profile of the diffraction lines (ND and XRD) of the materials showing a large amount of defects had to be fitted using the phenomenological anisotropic strain broadening model provided in the Fullprof suite for triclinic *P*-1 symetry[11,12,13] after deconvolution of the instrumental contribution determined from a $Na_2Ca_3Al_2F_{14}$ reference.

Vanadium K-edge X-ray absorption spectroscopy (XAS) spectra were acquired at room temperature in transmission mode at the ROCK beamline[14] of the synchrotron Soleil (France), using a vanadium foil as a reference for the energy calibration. The Si (111) quick-XAS

monochromator with an oscillating frequency of 2 Hz and an energy resolution of 0.2 eV was used for this experiment. The data were collected between 5330 and 6280 eV. Powder samples were mixed uniformly in a cellulose matrix and pressed into pellets of 13 mm diameter. Several X-ray absorption scans were collected to ensure the reproducibility of the spectra and to obtain high signal-to-noise ratio. The normalization, background subtraction and fit of the Extended X-Ray Absorption Fine Structure (EXAFS) oscillations were performed using the Demeter package[15].

Infrared (IR) vibrational spectroscopy was used to prove the presence of vanadyl-type environments and to demonstrate the absence of hydroxyl groups, often formed during the synthesis of fluorinated materials in aqueous media.[16] Diffuse reflectance measurements were performed in the mid-IR range (400−4000 cm^{-1}) using a FTIR Nicolet 6700 spectrometer (Thermo Scientific) equipped with a DTGS detector. The samples were finely ground in a mortar with dried KBr, the mass ratio between the active material and KBr being approximately 1:50. Finally, the reflectance spectra were treated with the Kubelka-Munk law, which converts the reflectance to a signal proportional to the absorption coefficient. Raman scattering measurements were performed with a Labram HR-800 micro-spectrometer (HORIBA Jobin Yvon). Spectra were recorded with a 514.5 nm excitation wavelength of an Ar^+ laser, with a power adjusted to ca. 50 µW in order to avoid any degradation of the sample.

The electrochemical tests were carried out in coin cells versus Lithium. The electrodes were prepared using 80 wt.% of active material, 10 wt.% of carbon (Super P) taking into account the carbon remaining from the synthesis and 10 wt.% of polyvinylidene fluoride (PVDF). N-methyl pyrrolidone was added to this mixture and the resultant slurry was cast on an Al foil and dried at 60°C during 24h. Discs of 12 mm diameter were cut in this foil, and after a drying at 80°C under vacuum during 24h these electrodes were cycled in galvanostatic mode in coin cells vs. metallic Lithium. The electrolyte used was a 1M solution of $LiPF_6$ in ethylene carbonate and dimethyl carbonate in a 1:1 volume ratio (LP30). Lithium cells were cycled, either in the high voltage domain between 3.0 and 4.6 V vs Li^+/Li (extraction of Lithium from $LiVPO_4F_{1-y}O_y$) or in the low voltage domain between 3.0 and 1.0 V vs Li^+/Li (insertion of Lithium into $LiVPO_4F_{1-y}O_y$).

2. Results

2a. Syntheses

The mixed valence (*i.e.* V^{III}/V^{IV}) phases were obtained through one-step solid state syntheses. First, V_2O_5, LiF and H_3PO_4 were dissolved in magnetically stirred distilled water at room temperature during 1h. After water evaporation at 80°C overnight, an excess of C_{sp} carbon (*i.e.* a highly divided soot) was added to the mixture. During the heating treatment (700°C, 1h under Argon) the carbon therefore acts as a reducing agent of the V^{5+} to yield V^{n+}-containing phases (with an average oxidation state n such as $3 \leq n \leq 4$). Therefore, the larger the excess of carbon introduced in the reaction medium, the smaller the oxidation state of vanadium in the final product. The samples obtained are labelled as LVPF-ε with ε referring to the molar excess of Carbon used for the syntheses (ε = 5, 25 or 50%). Let's note that the increase of carbon excess up to 50 mol.% doesn't allow to obtain a pure V^{3+}-containing phase and the decrease down to 5% leads to the formation of a $LiVPO_4O$-type phase as secondary phase. The SXRPD patterns of the three samples obtained are compared in **Figure 1** to those of the end member phases (*i.e.* $LiV^{IV}PO_4O$ and $LiV^{III}PO_4F$). All the main diffraction lines can be indexed in the Tavorite-type unit cell described in the triclinic (*P-1*) symmetry, with a minor impurity (< 2 wt.% of $Li_3V_2(PO_4)_3$ crystallizing in the anti-NASICON structure).

The corresponding SEM images (**Figure S1**) show that the primary particles of the mixed valence materials and of $LiVPO_4F$ are smaller compared to those of $LiVPO_4O$ (*i.e.* 0.5-1 μm for the first against 1-3 μm for $LiVPO_4O$), most probably due to the presence of carbon which for the former ones prevents the sintering of the particles during the annealing. These primary particles are aggregated into larger agglomerates, and small grains of carbon (50-100 nm), coming from the excess of carbon used during the syntheses, surround them.

Based on ICP-OES chemical analyses, the molar ratios Li/V/P were determined for all the samples. The results, given in the **Table 1**, are in good agreement with the expected compositions $LiVPO_4(O,F)$ (*i.e.* with 1Li:1V:1P). Nevertheless, the O/F ratio isn't reachable by ICP. However, this O/F ratio can be estimated by TGA coupled with MS under air. Indeed, as reported in ref. 17, under particular conditions it is possible to separate the weight losses assigned to carbon volatilization and to substitution of fluorine by oxygen in carbon surrounded $LiVPO_4F$. As shown in the TGA-MS data represented in **Figure S2**, three different temperature ranges were identified. A first weight loss assigned to adsorbed water

evaporation occurs below 350°C and corresponds to less than 1% in each sample. Between 350 and 500°C a second loss was identified, as associated with a detection of a signal on the CO_2 channel (*i.e.* m/z=44) whereas no significant HF release (m/z=20) is observed (**Figure S2b**). Thus, only carbon departure can be assigned to this weight loss and the carbon content determined for each sample is reported in **Table 1**. During the temperature plateau applied at 500°C for 1h, a third weight loss occurs accompanied by the detection of HF without any carbon release. Therefore, the weight percentage obtained allows determining the weight fraction of fluorine in the materials (also reported in **Table 1**).

In order to confirm the fluorine content thus obtained, which is related to the average oxidation state of vanadium, the magnetization of all materials was measured as a function of temperature in the paramagnetic domain (**Figure S3**). The average oxidation states of vanadium in each sample (reported in the **Table 1**) are found to be in good agreement with the compositions proposed based on the TGA-MS analyses and with the formation of mixed V^{3+}/V^{4+} valence materials: 3.75, 3.55 and 3.35 using respectively a molar excess of carbon of 5%, 25% and 50%. The compositions of LVPF-5%, LVPF-25% and LVPF-50% were thus assigned to $LiVPO_4F_{0.25}O_{0.75}$, $LiVPO_4F_{0.45}O_{0.55}$ and $LiVPO_4F_{0.65}O_{0.35}$ respectively, while it needs to be confirmed by the diffraction study.

2b. The crystallographic structure

The cell parameters of the three samples were determined by the Le Bail refinement based on the SXRPD data and they are reported in **Table 1**. Considering that the cell describing $LiVPO_4O$ is twice larger than that of $LiVPO_4F_{1-y}O_y$ ($y < 0.9$) (Figure S4), their cell parameters cannot be directly compared. Indeed, the main crystallographic feature of the Tavorite structure is the chains of transition metal octahedra sharing a corner and forming infinite X-V^{n+}-X-V^{n+}-X sequences (X = O^{2-} or F^- and n = 4 or 3). In $LiVPO_4F$, the bond lengths in this sequence are constant whereas for $LiVPO_4O$, due to the presence of V^{4+} and therefore of vanadyl bonds (*i.e.* covalent and short V^{IV}=O bonds), alternate short and long bond lengths are observed along the chains of octahedra. Therefore, for an easier comparison of the two different crystallographic cells, all the Tavorite-type samples are described in the $LiVOPO_4O$'s model. The evolution of the cell parameters as a function of the average oxidation state of vanadium determined by magnetic measurements is illustrated in the **Figure 2.** In this figure,

the data from the present study (filled symbols) are listed together with data either from other authors, [6, 18] either from one of our previous study[17] (open black symbols). The cell volumes follow a continuous evolution from $LiV^{IV}PO_4O$ (V/Z = 85.51 Å^3) [2] to $LiV^{III}PO_4F$ (V/Z = 87.14 Å^3) [2] with the increasing oxidation state of vanadium. Considering the V/Z values obtained for the three samples LVPF-5%, LVPF-25% and LVPF-50%, their chemical compositions would be $LiVPO_4F_{0.27}O_{0.73}$, $LiVPO_4F_{0.48}O_{0.52}$ and $LiVPO_4F_{0.65}O_{0.35}$, respectively. These compositions are in very good agreement with those previously estimated from the Curie constants. Interestingly, **Figure 2** highlights also that, contrarily to the cell volume, the cell parameters (especially $a_{LVPO\text{-}type}$ and $b_{LVPO\text{-}type}$) don't follow the Vegard's law given by the solid lines. Indeed, $b_{LVPO\text{-}type}$ is significantly smaller and $a_{LVPO\text{-}type}$ larger than predicted ones. In particular, the evolution of $a_{LVPO\text{-}type}$ and $b_{LVPO\text{-}type}$ parameters as a function of V^{n+} is rather linear from an average oxidation state of 3 to 3.90 for vanadium, and shows a significant deviation from linearity for higher oxidation states. Moreover, the phase transition between the cell with a multiplicity of 2 ($LiVPO_4F$-type, $0 \leq y < 0.9$ in $LiVPO_4F_{1-y}O_y$) and that with a multiplicity of 4 ($LiVPO_4O$-type, $y \geq 0.9$ in $LiVPO_4F_{1-y}O_y$) that is required to describe the ordering of vanadyl-type distortion coincides with the composition for which the deviation from the Vegard's law is maximum (*i.e.* an average oxidation state of vanadium ~ 3.9). Actually, the crystal field imposed by the highly ionic V-F bonds seems to prevent the ordering of the strongly covalent vanadyl bonds along the chains of octahedra (*i.e.* $\vec{b}_{LVPO-type}$ or $\vec{c}_{LVPF-type}$). The competition between the ionicity of the V^{3+}-F bond and the covalency of the V^{4+}=O bond is most probably at the origin of the deviation from the Vegard's law along their propagation directions. In order to compensate the framework shrinking induced by the increasing concentration of vanadyl-type bonds along the chains, an elongation occurs along the $\vec{a}_{LVPO-type}$ (or $(\vec{a} + \vec{b})_{LVPF-type}$) direction whereas no significant deviation has been detected along $\vec{c}_{LVPO}$ (or $(\vec{a} - \vec{b})_{LVPF-type}$).

An in-depth characterization of the average structure based on the analysis of synchrotron X-ray and neutron diffraction data was carried out in order to understand the deviation from the Vegard's law.

The profile and structure refinements have been done combining ND and SXRPD data, and considering a *P-1* triclinic unit cell of $LiVPO_4F$-type (Z = 2). Actually, both techniques are required to fully solve the structure and especially to localize the Lithium atoms and perform a careful analysis of the microstructure. Indeed, even if the angular resolution of ND is lower

than that of SXRPD, the higher scattering factors at high diffraction angles allow a better differentiation of the broadening induced by size and strain effects. The absence of superstructure peaks reveals a long range disordered O^{2-}/F^{-} and V^{3+}/V^{4+} distribution along the chains. The profiles of all these patterns are governed by a strong anisotropic strain broadening and must be refined using the corresponding model provided in the Fullprof software[13]. As already observed for that kind of materials [17,19], microstrains are mainly observed along the propagation direction of the chains of octahedra (*i.e.* [001] in the $LiVPO_4F$'s model), suggesting that they allow to accommodate the covalent and very short V^{4+}=O bonds as well as the ionic and longer V^{3+}-F ones, as disordered or even probably clustered, along this direction.

Rietveld refinements were performed considering the structural model $Li_{2i}(M(1))_{1a}(M(2))_{1b}\{(P)_{2i}[O_{2i}]_4\}X_{2i}$ already used to describe $LiVPO_4F$ and $LiVPO_4F_{1-y}O_y$ with $y \sim 0.75$.[2,6] The comparison of the experimental and calculated diffraction patterns (SXRPD and ND) is given as an example in **Figure 3** for the $LiVPO_4F_{0.45}O_{0.55}$ (LVPF-25%) composition. The corresponding cell parameters and atomic positions are gathered in **Table S1**. The crystal structure, illustrated in **Figure 4**, can be described as VO_4X_2 (with X = O or F) octahedra sharing common corners and forming $[X - VO_4 - X]_\infty$ chains along the [001] direction. These chains of octahedra are connected to each other via PO_4 tetrahedra, in such a way that each oxygen atom belonging to the VO_4 square plane of the VO_4X_2 octahedra is involved in a different phosphate group. The three-dimensional network thus generated accommodates Lithium atoms within the tunnels along the [100] direction. Since oxygen and fluorine are not differentiated either by X-ray or neutron diffraction, the Bond Valence Sums[20] (BVS) were calculated to determine the nature of the atoms which links the octahedra between them. The BVS value associated with the bridging anion was systemically found to be smaller (1.37(2)/1.60(2), 1.23(1)/1.42(1) and 1.22(1)/1.40(1) for F(1)/O(5) for y = 0.75, 0.55 and 0.35 in $LiVPO_4F_{1-y}O_y$ respectively) than those of the four other oxygen atoms (in average 1.94(2), 1.95(1), 1.91(1)). This result is in agreement with the structure already reported for other existing Tavorite-like fluoride phosphate phases,[2] with a fluorine atom bridging adjacent MO_4F_2 octahedra along the chains.

A comparison between the three mixed valence samples and the end-member phases (*i.e.* $LiV^{III}PO_4F$ and $LiV^{IV}PO_4O$) is interesting as it allows to understand the nature of the bonds observed along the chains of octahedra, depending on the bridging anion (*i.e.* F^- or O^{2-}) and

on the oxidation state of vanadium. In $LiV^{III}PO_4F$, the V-F distances along the chains built of $V(1)O_4F_2$ and $V(2)O_4F_2$ octahedra are almost constant (1.98 and 1.99 Å), with no asymmetry of the octahedra along the dz^2 orbitals of vanadium[2]. Conversely, due to the presence of V^{4+} in $LiV^{IV}PO_4O$, and to the formation of the vanadyl bonds, an alternation between short bonds (vanadyl bonds) at 1.62 or 1.71 Å and longer ones at 2.17 or 2.21 Å is observed[2]. This distortion of the octahedra around vanadium is thus at the origin of the lower symmetry observed for $LiV^{IV}PO_4O$, with a unit cell twice larger than that of $LiVPO_4F$. As reported in **Table 2**, as for $LiVPO_4F$, both V-X distances in a VO_4X_2 octahedron are symmetrically equivalent in the mixed valence materials $LiVPO_4F_{1-y}O_y$, with as expected a slight decrease of the average distance with an increasing content in oxygen (from 1.95 Å for y = 0.35 and to 1.93 Å for y = 0.75).

The BVS values associated with vanadium atoms for the three compositions discussed here are between 3 and 4 (**Table 2**), in good agreement with the formation of mixed V^{3+}/V^{4+} phases. Nevertheless, some divergences exist between the average oxidation states of vanadium cations determined by magnetic measurements (**Table 1**) and their BVS values (**Table 2**). In fact, only tiny differences are observed between the BVS values determined for vanadium atoms in these phases, whereas their average oxidation states were shown to be significantly different. Indeed, the V^{3+}-F/V^{4+}=O disorder involves then the formation of inhomogeneous distances along the chains. Therefore, the BVS calculations (performed considering the average description of the structure) are invalid in that case, due to a significant discrepancy between the actual local structure and the average structure.

The high covalency within phosphate groups generally generates highly rigid P−O distances[21], ranging here between 1.516(7) and 1.560(8) Å, and small tetrahedral distortion ($\Delta = 8.51 \times 10^{-5}$).

The Li site observed in the structure is surrounded by four oxygen atoms belonging to the square plane of four different VO_4X_2 octahedra and to one bridging anion, X (X = O or F), in a distorted LiO_4X polyhedron. The BVS values associated with Li in this site don't correspond to the theoretical value (*i.e.* 1, vs. 0.86(3), 0.89(3) and 0.88(3) respectively for $LiVPO_4F_{0.25}O_{0.75}$, $LiVPO_4F_{0.45}O_{0.55}$ and $LiVPO_4F_{0.65}O_{0.35}$) and the Debye-Waller factors (B_{iso}) associated are rather high (6.6(3), 3.7(3) and 3.0(3) respectively). Actually, the Li position might be impacted by the V^{3+}/V^{4+} and F^-/O^{2-} local disorder along the chains. The diffraction techniques, giving only an average position, balance the effect of a broad distribution for Li positions by artificially high

atomic displacement parameters, which are probably not correlated to the thermal motion of Lithium atoms around their equilibrium positions.

In the absence of superstructure peaks, a disordered F-V^{3+}/O=V^{4+}repartition along the chains seems to be formed. Diffraction giving only access to an average long range description, no information on the V-F bonds antagonist to vanadyl-type bonds (F-(V^{IV}=O)) and on the V-O bonds antagonist to the V-F ones (O-(V^{III}-F)) can be obtained from this technique. Nevertheless, it is essential to get direct information on these bonds as they may have a strong effect on the electronic configuration in vanadium's orbitals and *a fortiori* on the electrochemical properties. Spectroscopy experiments were thus needed to reveal the presence of the local vanadyl-type distortions predicted by DFT.[8]

2c. The local structure

Vibrational spectroscopy

The analysis of the whole series of $LiVPO_4F_{1-y}O_y$ compositions was performed by mid-Infrared absorption spectroscopy and Raman scattering to evidence the absence of hydroxyl groups and probe the V-O and P-O vibrations. The corresponding IR spectra are given in **Figure 5** whereas the vanadyl stretching region of the Raman scattering spectra are compared in supplementary information in **Figure S5**. In the 3000 - 4000 cm^{-1} region, no contribution was detected except for $LiVPO_4O$, for which a broad band is observed around 3400 cm^{-1} and assigned to the stretching vibration of adsorbed water, in agreement to the presence of the corresponding H-O-H bending mode at 1635 cm^{-1}.[22] The absence of signal for fluorinated materials in the O-H stretching region supports the compositions proposed without any substitution of fluorine by OH group. The PO_4 stretching region is located between 950 and 1200 cm^{-1}.[23,24] A single crystallographic site exists for phosphorus in $LiVPO_4F$, whereas two sites are identified in $LiVPO_4O$ (due to the lower symmetry and doubling of the unit cell). This induces an increase in the number of vibration modes in the PO_4 stretching region with the appearance of two bands around 1165 and 950 cm^{-1}, in addition to those observed for $LiVPO_4F$ (around 1120, 1050 and 1010 cm^{-1}). The PO_4 stretching region signature of the mixed valence samples is similar to that of $LiVPO_4O$, with weak additional contributions and broader signals. Otherwise, the vanadyl stretching mode is located at 915 cm^{-1} for $LiVPO_4O$.[23] This band is not expected for $LiVPO_4F$ which is theoretically a pure V^{3+}-containing material, and thus a vanadyl-

free composition. Nevertheless, a tiny peak is observed at 874 cm^{-1}, shifted versus the vanadyl stretching mode observed for $LiVPO_4O$, but matching with the presence of local vanadyl-type defects in $LiVPO_4F$.[17] As the average oxidation state of vanadium is increased, a slight shift towards higher wavenumbers and an increasing amplitude of the vanadyl-type signal are observed: Note that the intensity of the vanadyl vibration doesn't evolve linearly with the O^{2-}/F^- ratio, the presence of fluorine might disrupt the formation of the vanadyl environment ($O=V^{4+}$--O) and inhibit the corresponding vibration. Moreover, several shoulders are detected around 900, 865 and 825 cm^{-1} which could be induced by the broad distribution of V^{4+}=O environments. Raman scattering (**Figure S5**) reveals contributions, assigned to the vanadyl bond[25], around 875 cm^{-1} for each sample. Weaker ones, at slightly higher wavenumber (~911 cm^{-1}), are also observed for mixed valence materials with a broadening of the signal. That is most probably due to the wide distribution of X-V^{4+}=O environments in these materials. However, the V^{4+}=O bond lengths estimated from the Raman wavenumber[25] were found to be close (i.e. 1.66 Å for 875 cm^{-1} and 1.65 Å for 910 cm^{-1} vibrations) whatever the oxygen substitution ratio for fluorine. It suggests a very robust vanadyl bond, almost not really affected by its chemical environment.

IR spectroscopy and Raman scattering have confirmed the formation of the vanadyl bonds in $LiVPO_4F_{1-y}O_y$, which is in good agreement with the predictions previously obtained from DFT calculations[8]. In order to obtain further insights on the different local environments around V atoms, X-ray absorption experiments have been conducted at the V K-edge.

X-ray Absorption Spectroscopy

X-ray absorption spectra were recorded at the vanadium K-edge to probe the vanadium oxidation state and local structure around the absorber. **Figure 6a** displays the spectra recorded for the series of $LiVPO_4F_{1-y}O_y$ materials.

The pre-edge absorption feature P, located between 5466.0 and 5474.0 eV (inset of **Figure 6a**) is followed by a weak shoulder (A) on the rising absorption edge which culminates in a strong peak (B). This strong peak B is assigned as the dipole-allowed transition 1s to 4p,[26] and the pre-edge feature P as the transition 1s to 3d.[26] This latter is strictly forbidden in perfectly regular vanadium octahedra but becomes dipole allowed with the distortion of the local symmetry around the absorber, which leads to a 3d-4p orbital mixing and thus to an

overlap of the metal 3d orbitals with the 2p orbitals of the ligands.[26] Therefore, this pre-edge region is highly sensitive to the local distortions around vanadium and gives insights into its local environments. Actually, two weak contributions are distinguished in the feature P for $LiVPO_4F$. At a first sight, these contributions can be assigned to the 1s-t_{2g} transition at 5468.0 eV and to the 1s-e_g one at 5469.7 eV resulting from the vanadium's orbitals splitting with a crystal field of 1.7 eV. Since this latter is close (*i.e.* shifted of only 0.3 eV) to the contribution of V^{4+} involved in a vanadyl-type bond as in $LiVPO_4O$[26,27], it could thus arise from both the contribution of vanadyl-type defects {V^{4+}=O} and the 1s-e_g transition of V^{3+}. This contribution at 5469.7 eV grows in intensity with the rise of the vanadium oxidation state and thus the concentration of vanadyl-type environments in the materials. **Figure 6b** shows the evolution of the pre-edge integrated intensity and of the edge position (taken at half jump) as a function of the vanadium average oxidation state, both of them evolving not linearly between the values of the two end members, $LiV^{III}PO_4F$ and $LiV^{IV}PO_4O$ (dashed lines). The intensity of the pre-edge is significantly smaller than expected for a linear evolution for the intermediate compositions, whereas the shift of the edge position towards higher energy is larger. The presence of strongly ionic V-F bonds appears to inhibit the formation of "true" vanadyl-type environments ($O=V^{4+}$--O), in good agreement with the structure of these mixed valence $LiVPO_4F_{1-y}O_y$ materials, described in a LVPF-type model and not in a LVPO-type, even for small fluorine contents. Moreover, the edge position does not evolve linearly with the vanadium average oxidation state, as it is affected by both the V^{4+}/V^{3+} ratio and the iono-covalent character of the V-X bonds.[28] It appears again that the competition between the formation of strongly ionic V^{3+}-F bonds at the expense of strongly covalent {V^{4+}=O} ones, already proposed to explain the offset from the Vegard's law, could be at the origin of this non-linear behavior at the electronic level.

The analysis of the EXAFS oscillations will then help us to clarify the nature of the atoms belonging to the coordination sphere of V and the distances between them. In our case, as O^{2-} and F^- interact similarly with X-rays, only the distances between vanadium and its ligands can be probed. The complexity of the systems studied here (disordered triclinic compounds) is limiting the description of the far coordination shells. Thus, only the first coordination sphere around vanadium will be discussed here. The fits in the R space of the Fourier transforms of the k^2-weighted V K-edge EXAFS oscillations (k-range: 3.7-11.0 $Å^{-1}$, sine window) are given in supplementary information in **Figure S6**. In these conditions, the number of independent

parameters is limited to 6 (~ 2.Δk.ΔR/π) [27]. The local environment around vanadium in $LiVPO_4F$ can be described as 6 equivalent ligands located at 2.00(1) Å away from V atom (*vs.* 1.971(2) Å in average from XRD). The tiny amount of defects in this sample doesn't contribute significantly to the EXAFS oscillations contrarily to the vanadyl bond in $LiVPO_4O$. For $LiVPO_4O$ sample, a model based on the 1+4+1 coordination is clearly needed to take into account the vanadyl distortion. The shorter V^{4+}=O bond length is 1.64(1) (*vs.* 1.626(3) Å from XRD) the four others being 2.00(3) (*vs.* 1.986(3) Å in average from XRD) and the longest one is 2.25(3) (*vs.* 2.239(3) Å from XRD) leading to BVS values of 3.83 from EXAFS against 3.93 from XRD. In both cases the results obtained from XRD and EXAFS are in very good agreement, showing that the average structural description given by XRD is representative of the structure. For the mixed valence phases $LiVPO_4F_{1-y}O_y$ three different local environments can be observed, with different probabilities depending on the F^-/O^{2-} substitution ratio (*i.e.* y) (see **Figure 7** and **Table S2**). We assume a constant 6-fold coordination for vanadium with the following constraints:

(i) All V^{4+} forming a short vanadyl bond with an oxygen, with a probability $p_i = y/6$, y referring to y in $LiVPO_4F_{1-y}O_y$.

(ii) Long antagonist V^{4+}--O bonds are formed along the chains with the following probability: $p_{ii} = (y^2/(2-y))/6$.

(iii) All the other bonds (i.e. V^{3+}-X (X = O or F), V^{4+}-F and V^{4+}-O (these latter belonging to the square plane of $V^{4+}O_4X_2$)) were shown, refined independently, to be equivalent. The probability for this distance V-X is $p_{iii} = (6-y-y^2/(2-y))/6$.

This leads to a coordination such as $[(6 * p_i)_{V4+=O}] + [(6 * p_{ii})_{V4+--O}] + [(6 * p_{iii})_{V-X}]$. The number of V^{4+}=O and V^{4+}--O bonds are thus fixed to 0.75 and 0.45, 0.55 and 0.20, 0.35 and 0.1 for $LiVPO_4F_{0.25}O_{0.75}$, $LiVPO_4F_{0.45}O_{0.55}$ and $LiVPO_4F_{0.65}O_{0.35}$ respectively (see **Figure 7**). The vanadyl V^{4+}=O bond length is found to be 1.64(1) Å and the antagonist V^{4+}--O bond around 2.2 Å. The coordination of vanadium is completed considering 4.8, 5.25 and 5.55 additional V-X bonds (*i.e.* $6*p_{iii}$, for $LiVPO_4F_{0.25}O_{0.75}$, $LiVPO_4F_{0.45}O_{0.55}$ and $LiVPO_4F_{0.65}O_{0.35}$ respectively), found to be distant of 2.01(1) Å. The description of the distorted vanadium local environment detailed in **Table S2** clearly doesn't match with the centrosymmetric VO_4X_2 octahedra identified by diffraction. However, the presence of distorted VO_4X_2 octahedra is doubtless identified by the intense pre-peak P. The average distances around vanadium obtained from XRD are in good agreement with those obtained from EXAFS. Interestingly, the distances obtained from EXAFS

(contrarily to those obtained from XRD) provide BVS values close to those expected considering the average vanadium oxidation state determined by magnetic measurements. From the EXAFS point of view, the sequences of octahedra in the three mixed valence materials $LiVPO_4F_{1-y}O_y$ can be described as a sum of three distinct vanadium environments (*i.e.* X-$V^{3+}O_4$-X, F-$V^{4+}O_4$=O and O-$V^{4+}O_4$=O) whose proportions vary, but almost not affected in their distances whatever their surroundings. **Figure 7** illustrates a schematic description considering the EXAFS results and the gap with the Vegard's law mainly observed along the propagation direction of the chains of octahedra (along $\vec{b}_{LVPO}$ or $\vec{c}_{LVPF}$). Indeed, in a conventional solid solution, a mixture of end-member-type environments is expected whereas, in our case, a third environment is stabilized. Although X-$V^{3+}O_4$-X and O-$V^{4+}O_4$=O environments are very similar to those observed in $LiVPO_4F$ and $LiVPO_4O$ respectively, the F-$V^{4+}O_4$=O octahedron is shrunk along the dz^2 orbitals of vanadium. The formation of the vanadyl bond is observed, but the presence of fluorine prevents the formation of the longer antagonist bond, leading to a compaction of these $V^{4+}O_4OF$ octahedra and to a shortening of the b_{LVPO} $(or\ c_{LVPF})$ cell parameter. Moreover, the probability for the presence of shrunk F-$V^{4+}O_4$=O octahedra (*i.e.* $p = y-y^2/(2-y)$) fits very well with the amplitude of the offset from the Vegard's law observed along the $\vec{b}_{LVPO}$ $(or\ \vec{c}_{LVPF})$ direction (see **Figures 2 and 7**) as a function of the average oxidation state of vanadium.

The structural description proposed from EXAFS results describes the local environments of the disordered mixed valence materials $LiVPO_4F_{1-y}O_y$, in good agreement with the DFT calculations. The local environments around vanadium being different from those observed in the end-member phases, the electrochemical properties should be strongly impacted by the F^-/O^{2-} (and V^{3+}/V^{4+}) ratio.

2d. The electrochemical properties

We suspect that all $LiVPO_4F$ reported in literature present various amount of vanadyl-type defects influencing the electrochemical performance.[7] In fact, the electrochemical performance might closely depend on their concentrations/distributions in a similar way than the carbon coating or the particles' sizes. In this part we will discuss about the influence of the vanadyl-type environments on the electrochemical properties. The ability of vanadium to be

stabilized in various oxidation states allows to play with the V^{2+}/V^{3+}, V^{3+}/V^{4+} and V^{4+}/V^{5+} redox couples, by either inserting or extracting Lithium into/from $LiVPO_4F_{1-y}O_y$. Recently, this system has been investigated as multi-electron materials[6] (exchanging ~1.6 electron per transition metal), but due to the complex processes involved in the two reactions (*i.e.* insertion and extraction) we decided to investigate them separately in the low and high voltage domains as shown in **Figure 8**.

Low voltage signature as a local probe

In the low voltage region (*i.e.* 3.0 - 1.5 V *vs.* Li^+/Li), the Lithium insertion into $LiVPO_4F$ occurs at 1.8 V according to a biphasic process between $LiVPO_4F$ and Li_2VPO_4F involving the V^{III}/V^{II} redox couple[29]. The Lithium insertion into $LiVPO_4O$ leads to the reduction of V^{IV} to V^{III} according to a complex series of phase transitions occurring at 2.48 V, 2.31 V and 2.03 V *vs.* Li^+/Li, to reach the composition $Li_2V^{III}PO_4O$.[30,31] **Figure 8b** shows the galvanostatic curves of the mixed valence materials cycled in the 3.0 – 1.0 V *vs.* Li^+/Li voltage range (involving the V^{II}/V^{III} and V^{III}/V^{IV}=O redox couples) at C/10. The voltage profile of the mixed valence samples $LiVPO_4F_{1-y}O_y$ can be described as a combination of a $LiVPO_4O$-type signature above 1.9 V, a $LiVPO_4F$-type signature between 1.9 and 1.6 V and a third unknown contribution at lower potential (*i.e.* 1.4 V *vs.* Li^+/Li, see inset of **Figure 8b**). Moreover, the relative proportions of each contribution evolve as a function of the O^{2-}/F^- ratio. Indeed, by increasing the fluorine content, the length of the $LiVPO_4F$-type pseudo-plateau increases. Regarding the third unknown contribution, it could correspond either to the further reduction of V^{3+} in an oxygen-rich environment (*i.e.* O-V^{3+}-O to O-V^{2+}-O) or to the reduction of V^{3+} in a mixed fluorine-oxygen environment (*i.e.* O-V^{3+}-F to O-V^{2+}-F). To the best of our knowledge, the further insertion of Lithium into $Li_2V^{III}PO_4O$ has never been reported and the corresponding voltage is thus unknown. However, the pseudo-plateau observed for $LiVPO_4F_{1-y}O_y$ samples appears at a voltage close to the one measured for the V^{2+}/V^{3+} redox couple in $Li_{1+x}VPO_4OH$ (*i.e.* 1.40 V against 1.35 V *vs.* Li^+/Li in $LiVPO_4OH$[32]). This contribution at 1.40 V vs. Li^+/Li cannot be assigned to the presence of OH groups whose absence has already been demonstrated by IR spectroscopy. However, the voltage of an eventual reduction of V^{3+} in oxygen-rich environment should be located close to 1.35 V *vs.* Li^+/Li. Another hypothesis explaining this contribution is to consider the reduction of V^{3+} in a mixed fluorine-oxygen environment,

whose redox potential is expected to be located at slightly lower voltage than V^{2+}/V^{3+} redox couple in $Li_{1+x}VPO_4F$ (*i.e.* 1.8 V *vs.* Li^+/Li) due to the lower electronegativity of O^{2-} compared to F^-.

Although the Lithium insertion reaction isn't interesting from an application's point of view because of its low voltage, the corresponding electrochemical signature appears as a local probe, which supports the local structural description of the materials that we previously proposed and it is thus useful to estimate easily the amount of vanadyl-type defects in the materials.

<u>High voltage</u>

Figure 8a gathers the galvanostatic data and the corresponding derivative curves obtained for the mixed valence materials cycled in the 3.0 – 4.6 V *vs.* Li^+/Li voltage range (involving the V^{3+}/V^{4+} and V^{4+}/V^{5+} redox couples) at C/10. In this voltage region, the Lithium extraction from $LiVPO_4F$ corresponds to the oxidation of V^{III} to V^{IV} whereas the V^{IV}/V^{V} redox couple is involved for $LiVPO_4O$. The Lithium deintercalation from $LiVPO_4F$ occurs at an average voltage of 4.25 V *vs.* Li^+/Li while it occurs at a lower potential (3.95 V *vs.* Li^+/Li for V^{IV}/V^{V}) for $LiVPO_4O$[2]. Actually, for that latter, due to the presence of vanadyl bonds, the redox couple involved is the $\{V=O\}^{2+}/\{V=O\}^{3+}$ one and the presence of this strongly covalent bond acts as a "reverse inductive effect" which tends to decrease significantly the voltage of the V^{4+}/V^{5+} redox couple in $LiVPO_4O$. From $LiVPO_4O$ to VPO_4O, the extraction mechanism involved is a single biphasic reaction[30]. For $LiVPO_4F$, a more complex mechanism occurs with the formation of an intermediate $Li_{0.67}VPO_4F$ composition during charge which isn't observed during discharge[29]. Similarly to the electrochemical process involved for $LiVPO_4F$, those associated with $LiVPO_4F_{1-y}O_y$ samples seem to be asymmetric. For instance, three peaks are observed at 4.21, 4.25 and 4.27 V *vs.* Li^+/Li on the derivative curve of the first charge of the $Li//LiVPO_4F_{0.65}O_{0.35}$ cell whereas only one asymmetric peak can be detected during the following discharge (at 4.19 V *vs.* Li^+/Li). Additional peaks are observed on the derivative curve of $LiVPO_4F_{0.45}O_{0.55}$ (at 3.6, 3.7 and 4.1V *vs.* Li^+/Li): they correspond to the contribution of the electrochemically active $Li_3V_2(PO_4)_3$ impurity[33].

Figure 8a reveals, additionally, a clear decrease of the irreversible capacity as the fluorine content in the materials is increased conferring to the fluorine rich materials a higher reversible capacity. Moreover, the polarization tends to decrease (*i.e.* 130 mV, 100 mV and 70

mV respectively for y = 0.75, 0.55 and 0.35 in $LiVPO_4F_{1-y}O_y$) and the average voltage tends to increase with the rise of the fluorine content in the material (*i.e.* 4.13 V, 4.20 V and 4.22V *vs.* Li^+/Li respectively for y = 0.75, 0.55 and 0.35 in $LiVPO_4F_{1-y}O_y$). From these observations, it appears that the fluorine rich mixed valence materials deliver the better performance, to be compared with that of $LiVPO_4F$. **Figure 9** shows the evolution of the discharge capacity as a function of the cycling number at various C-rates (*i.e.* 5 cycles at C/10, C/5, C/2, C, 2C, C, C/2, C/5, C/10 and then 50 cycles at C) for $LiVPO_4F_{1-y}O_y$ materials (with y between 0 and 0.75). The $LiVPO_4F$ given for comparison in this figure is a quasi-stoichiometric one obtained by a different synthesis (described in the experimental part) whose morphology and "Carbon coating" are very similar to those of mixed valence phases (see **Figure S1**). Even if the initial reversible capacity at low rate of $LiVPO_4F$ is the highest of the studied materials (122, 109, 102, 89 mAh/g respectively from y = 0 to 0.75), its capacity retention and rate capability decrease faster. Indeed after 5 cycles at C/10 a loss of 20% of the reversible capacity is observed for $LiVPO_4F$ whereas no significant decrease is observed for the mixed valence materials. Moreover, as the rate is increased, the reversible capacity delivered by $LiVPO_4F$ decreases strongly until reaching 15mAh/g at 2C whereas at this rate the capacity provided by the $LiVPO_4F_{1-y}O_y$ samples is several times larger (62, 55 and 40 mAh/g respectively for y = 0.35 to 0.75).

However, the performance delivered by our $LiVPO_4F$ sample are rather poor compared to the better ones reported in literature[3,34]. The too low amount of defects in our $LiVPO_4F$ samples could be the reason. But, in such kind of materials with low electronic conductivity, the optimization of the carbon coating and of the particles' size is essential and there is no doubt that they aren't optimal in our samples. In any case, the materials compared in this work present similar coating and particle's sizes and the performance delivered by the mixed valence samples is better than those of the stoichiometric material and even better when their fluorine content increases. Therefore, it would seem that an optimal vanadyl-type defects' concentration (located between the $LiVPO_4F_{0.65}O_{0.35}$ and the $LiVPO_4F$ compositions) exists which would improve the transport properties. Actually, for high voltage materials such as $LiVPO_4F$, the charge capacity is often limited by the polarization which makes that the cut-off voltage (*i.e.* 4.6 V *vs.* Li^+/Li, stability limit of the classical electrolytes) is reached before the reaction is completed. Indeed, many works reported high discharge capacity at high rate after

low charge rate[5,35]. Therefore, the decrease of the polarization and voltage by introducing vanadyl-type defects in the $LiVPO_4F$ structure benefits to the rate capability.

The decrease of the polarization can originate from the enhancement of either electronic or cationic mobility. Typically, the mixed valence states of the transition metals can increase the electronic conductivity by enhancing the hopping process between cations with different oxidation states. This was recently observed in the mixed valence phase $Na_3V_2(PO_4)_2F_{2.5}O_{0.5}$ for which a significant improvement of the electronic conductivity has been evidenced compared to that of the pure V^{3+} phase (*i.e.* $Na_3V_2(PO_4)_2F_3$)[36]. Furthermore, the distortion of the Tavorite network due to the competition between V^{3+}-F and V^{4+}=O (at the origin of the non-Vegard's law behavior) could open new diffusion paths for Lithium and thus improve the ionic transport properties. Finally, the complex series of phase transitions and the corresponding redox mechanisms involved in $Li_xVPO_4F_{1-y}O_y$ upon Lithium de-intercalation and re-intercalation could also influence greatly their electrochemical properties. These mechanisms are under study, in order to determine the origin of the performance improved with the introduction of vanadyl-type defects in $LiVPO_4F$: it will be the subject of an up-coming article.

Conclusion

This work is part of a series of studies conducted in our groups and dealing with vanadyl-type defects in vanadium fluoride phosphate materials ($LiVPO_4F$ [7,8,17] and $Na_3V_2(PO_4)_2F_3$ [27,36]). The combination of advanced characterizations by diffraction and spectroscopy allowed an in-depth understanding of the $LiVPO_4F_{1-y}O_y$ phases, from their long range average structure to their local one. Beyond the fundamental interest offered by the rich crystal chemistry induced by the competition between the ionicity of the V^{3+}-F bond and the covalency of the V^{4+}=O bond, these phases attract a real interest as positive electrode materials for Li-ion batteries. We found that the electrochemical properties are correlated to the vanadyl type defects' concentration, and the careful control of the composition thus allows a significant improvement of the performance in batteries. Many studies dealing with $LiVPO_4F$ mention coating or particles' size as the only parameters impacting its electrochemical behavior, and defects were rarely reported as such. This study also demonstrates that the amount of vanadyl-type defects in $LiVPO_4F$-type phases can be easily evaluated by the low voltage signature (*i.e.* activation of the V^{3+}/V^{2+} redox couple

of $LiVPO_4F$). In the future, in order to be more critical on the contribution of the vanadyl-type defects into the performance reported for $LiVPO_4F$ and to compare more easily the $LiVPO_4F$-type materials between them, the authors should thus provide the low voltage signature.

Acknowledgment

The authors thank Michel Ménétrier, Marie Guignard, Patrick Rosa, Cathy Denage, Laetitia Etienne and Eric Lebraud at ICMCB and Matthieu Courty at LRCS for discussions and support in running some technical experiments, as well as ALBA (Barcelona, Spain) for Synchrotron X-ray diffraction experiments on MSPD beamline, ILL (Grenoble, France) for neutron diffraction experiments on the D2B diffractometer, and SOLEIL (Gif-sur-Yvette, France) for X-ray spectroscopy experiments on ROCK beamline (financed by the French National Research Agency (ANR) as a part of the "Investissements d'Avenir" program, reference: ANR-10-EQPX-45; proposal number 20160282). The authors also acknowledge FEDER, the Région Hauts-de-France and the RS2E Network for the funding of EB's PhD thesis, as well as the financial support of Région Nouvelle Aquitaine and of the French National Research Agency (STORE-EX Labex Project ANR-10-LABX-76-01 and HIPOLITE Progelec project ANR-12-PRGE-0005-02).

References

(1) Masquelier, C.; Croguennec, L. Polyanionic (Phosphates, Silicates, Sulfates) Frameworks as Electrode Materials for Rechargeable Li (or Na) Batteries. *Chem. Rev.* **2013**, *113* (8), 6552–6591.

(2) Ateba-Mba, J. M.; Masquelier, C.; Suard, E.; Croguennec, L. Synthesis and Crystallographic Study of Homeotypic $LiVPO_4F$ and $LiVPO_4O$. *Chem. Mater.* **2012**, *24*, 1223–1234.

(3) Huang, H.; Faulkner, T.; Barker, J.; Saidi, M. Y. Lithium Metal Phosphates, Power and Automotive Applications. *J. Power Sources* **2009**, *189*, 748–751.

(4) Zheng, J.; Zhang, B.; Yang, Z. Novel Synthesis of $LiVPO_4F$ Cathode Material by Chemical Lithiation and Postannealing. *J. Power Sources* **2012**, *202*, 380–383.

(5) Xiao, P. F.; Lai, M. O.; Lu, L. Transport and Electrochemical Properties of High Potential Tavorite $LiVPO_4F$. *Solid State Ionics* **2013**, *242*, 10–19.

(6) Kim, M.; Lee, S.; Kang, B. High Energy Density Polyanion Electrode Material ; $LiVPO_4O_{1-x}Fx$ (X ≈ 0.25) with Tavorite Structure. *Chem. Mater.* **2017**, *29* (11), 4690–4699.

(7) Messinger, R. J.; Ménétrier, M.; Salager, E.; Boulineau, A.; Duttine, M.; Carlier, D.; Ateba Mba, J.-M.; Croguennec, L.; Masquelier, C.; Massiot, D.; et al. Revealing Defects in Crystalline Lithium-Ion Battery Electrodes by Solid-State NMR: Applications to $LiVPO_4F$. *Chem. Mater.* **2015**, *27*, 5212–5221.

(8) Bamine, T.; Boivin, E.; Boucher, F.; Messinger, R. J.; Salager, E.; Deschamps, M.; Masquelier, C.; Croguennec, L.; Ménétrier, M.; Carlier, D. Understanding Local Defects in Li-Ion Battery Electrodes through Combined DFT/NMR Studies: Application to $LiVPO_4F$. *J. Phys. Chem. C* **2017**, *121* (6), 3219–3227.

(9) Bain, G. a.; Berry, J. F. Diamagnetic Corrections and Pascal's Constants. *J. Chem. Educ.* **2008**, *85* (4), 532–536.

(10) Fauth, F.; Peral, I.; Popescu, C.; Knapp, M. The New Material Science Powder Diffraction Beamline at ALBA Synchrotron. *Powder Diffr.* **2013**, *28*, 360–370.

(11) Rodriguez-carvajal, J. Recent Advances in Magnetic Structure Determination by Neutron Powder Diffraction. *Phys. B* **1993**, *192*, 55–69.

(12) Stephens, P. W. Phenomenological Model of Anisotropic Peak Broadening in Powder Diffraction. *J. Appl. Crystallogr.* **1999**, *32*, 281–289.

(13) Rodríquez-Carvajal, J.; Roisnel, T. Line Broadening Analysis Using FullProf: Determination of Microstructural Properties. *Mater. Sci. Forum* **2004**, *443*, 123–126.

(14) Briois, V.; La Fontaine, C.; Belin, S.; Barthe, L.; Moreno, T.; Pinty, V.; Carcy, A.; Girardot, R.; Fonda, E. ROCK : The New Quick-EXAFS Beamline at SOLEIL. *J. Phys. Conf. Ser.* **2016**, *712*, 1–6.

(15) Ravel, B.; Newville, M. ATHENA, ARTEMIS, HEPHAESTUS: Data Analysis for X-Ray Absorption Spectroscopy Using IFEFFIT. *J. Synchrotron Radiat.* **2005**, *12*, 537–541.

(16) Ellis, B. L.; Nazar, L. F. Anion-Induced Solid Solution Electrochemical Behavior in Iron Tavorite Phosphates. *Chem. Mater.* **2012**, *24*, 966–968.

(17) Boivin, E.; Chotard, J. N.; Ménétrier, M.; Bourgeois, L.; Bamine, T.; Carlier, D.; Fauth, F.; Masquelier, C.; Croguennec, L. Oxidation under Air of Tavorite $LiVPO_4F$: Influence of Vanadyl-Type Defects on Its Electrochemical Properties. *J. Phys. Chem. C* **2016**, *120*, 26187–26198.

(18) Onoda, M.; Ishibashi, T. Phase Transition and Spin Dynamics of the $LiVFPO_4$ Insertion Electrode with the S = 1 Linear Chain and the Development of F – O Mixed System. *J. Physial Soc. Japan* **2015**, *84*, 1–5.

(19) Boivin, E.; Chotard, J.-N.; Bamine, T.; Carlier, D.; Serras, P.; Veronica, P.; Rojo, T.; Iadecola, A.; Dupont, L.; Bourgeois, L.; et al. Vanadyl-Type Defects in Tavorite-like $NaVPO_4F$: From the Average Long Range Structure to Local Environments. *J. Mater. Chem. A* **2017**, *5*, 25044–25055.

(20) Brown, I. D.; Altermatt, D. Bond-Valence Parameters Obtained from a Systematic Analysis of the Inorganic Crystal Structure Database I . *Acta Cryst* **1985**, *41*, 244–247.

(21) Huminicki, D. M. C.; Hawthorne, F. C. The Crystal Chemistry of the Phosphate Minerals. *Rev. Mineral. Geochemistry* **2002**, *48* (1), 123–253.

(22) Nakamoto, K. *Infrared and Raman Spectra of Inorganic and Coordination Compounds. Part B: Applications in Coordination, Organometallic, and Bioinorganic Chemistry*; John Wiley & Sons, Inc., 1997.

(23) Harrison, K. L.; Manthiram, A. Microwave-Assisted Solvothermal Synthesis and Characterization of Various Polymorphs of $LiVOPO_4$. *Chem. Mater.* **2013**, *25*, 1751–1760.

(24) Marx, N.; Croguennec, L.; Carlier, D.; Bourgeois, L.; Kubiak, P.; Cras, F. Le; Delmas, C. Structural and Electrochemical Study of a New Crystalline Hydrated Iron(III) Phosphate $FePO\ 4 \cdot H\ 2\ O$ Obtained from $LiFePO_4(OH)$ by Ion Exchange. *Chem. Mater.* **2010**, *22*, 1854–1861.

(25) Hardcastle, F. D.; Wachs, I. E. Determination of Vanadium-Oxygen Bond Distances and Bond Orders by Raman Spectroscopy. *J. Phys. Chem. C* **1991**, *95* (13), 5031–5041.

(26) Wong, J.; Lytle, F.W.; Messmer, R.P. and Maylotte, D. H. K-Edge Absorption Spectra of Selected Vanadium Compounds. *Phys. Rev. B* **1984**, *30* (10), 5596–5610.

(27) Broux, T.; Bamine, T.; Fauth, F.; Simonelli, L.; Olszewski, W.; Marini, C.; Ménétrier, M.; Carlier, D.; Masquelier, C.; Croguennec, L. Strong Impact of the Oxygen Content in $Na_3V_2(PO_4)_2F_{3-y}O_y$ ($0 \leqq Y \leqq 0.5$) on Its Structural and Electrochemical Properties. *Chem. Mater.* **2016**, *2*, acs.chemmater.6b02659.

(28) Ghatikar, M. N.; Padalia, B. D. Empirical Relations and the X-Ray Absorption Edge-Shifts. *J. Phys. C Solid State Phys.* **1978**, *11*, 1941–1955.

(29) Ateba Mba, J.-M.; Croguennec, L.; Basir, N. I.; Barker, J.; Masquelier, C. Lithium Insertion or Extraction From/into Tavorite-Type $LiVPO_4F$: An In Situ X-Ray Diffraction Study. *J. Electrochem. Soc.* **2012**, *159* (8), A1171–A1175.

(30) Bianchini, M.; Ateba Mba, J. M.; Dagault, P.; Bogdan, E.; Carlier, D.; Suard, E.; Masquelier, C.; Croguennec, L. Multiple Phases in the ε-VPO_4O–$LiVPO_4O$–Li_2VPO_4O System: A Combined Solid State Electrochemistry and Diffraction Structural Study. *J. Mater. Chem. A* **2014**, *2*, 10182.

(31) Lin, Y.; Wen, B.; Wiaderek, K.; Sallis, S.; Liu, H.; Lapidus, S.; Borkiewicz, O.; Quackenbush,

N.; Chernova, N.; Karki, K.; et al. Thermodynamics, Kinetics and Structural Evolution of ε -$LiVOPO_4$ over Multiple Lithium Intercalation. *Chem. Mater.* **2016**, *28*, 1794–1805.

(32) Boivin, E.; Chotard, J.-N.; Ménétrier, M.; Bourgeois, L.; Bamine, T.; Carlier, D.; Fauth, F.; Suard, E.; Masquelier, C.; Croguennec, L. Structural and Electrochemical Studies of a New Tavorite Composition $LiVPO_4OH$. *J. Mater. Chem. A* **2016**, *4*, 11030–11045.

(33) Yin, S.-C.; Grondey, H.; Strobel, P.; Anne, M.; Nazar, L. F. Electrochemical Property : Structure Relationships in Monoclinic $Li_{3-y}V_2(PO_4)_3$. *J. Am. Chem. Soc.* **2003**, *2* (11), 10402–10411.

(34) Kim, M.; Lee, S.; Kang, B. Fast-Rate Capable Electrode Material with Higher Energy Density than $LiFePO_4$: 4.2V $LiVPO_4F$ Synthesized by Scalable Single-Step Solid-State Reaction. *Adv. Sci.* **2015**, 1–9.

(35) Wang, Y.; Zhao, H.; Ji, Y.; Wang, L.; Wei, Z. Long-Life and High-Rate $LiVPO_4F$/C Nanocrystals Modified with Graphene as Cathode Material for Lithium-Ion Batteries. *Solid State Ionics* **2014**, *268*, 169–173.

(36) Broux, T.; Fleutot, B.; David, R.; Brüll, A.; Veber, P.; Fauth, F.; Courty, M.; Croguennec, L.; Masquelier, C. Temperature Dependence of Structural and Transport Properties for $Na_3V_2(PO_4)_2F_3$ and $Na_3V_2(PO_4)_2F_{2.5}O_{0.5}$. *Chem. Mater.* **2017**, 0–27.

Table captions

Table 1: cell parameters determined from Le Bail refinement on Synchrotron XRPD data with the corresponding chemical analyses performed by ICP-OES (Li, V and P) or TGA (C and F content), and magnetic parameters determined from the $1/\chi_m = f(T)$ curves (χ_m = magnetic susceptibility, T = temperature) at a magnetic field H of 10 kOe.

Table 2: Significant bond lengths (Å) obtained for the $LiVPO_4F_{1-y}O_y$ materials from the combined Rietveld refinement based on the SXRPD and ND data. Polyhedral distortion is calculated as $\Delta=\frac{1}{N}\sum_{i=0}^{N}\frac{(di-\langle d\rangle)^2}{\langle d\rangle^2}$ with N the number of bond distances considered, d_i the distance between the atom i and the central atom of the polyhedron and ‹d› the average of the distances considered.

Figure captions

Figure 1: Synchrotron XRD patterns of the $LiVPO_4F_{1-y}O_y$ series of materials.

Figure 2: Evolution of the cell parameters (a, b and c as triangles, squares and circles respectively) and of the cell volumes (V/Z as stars) in a $LiVPO_4O$-type model (Z = 4) as a function of the average oxidation state of vanadium for $LiVPO_4F_{1-y}O_y$ compositions. Those appearing as filled and colored symbols are at the center of this paper, whereas those appearing as black and empty symbols are already reported in literature, either by other authors [6, 18] or by us [17]. The red-filled area corresponds to the range of compositions for which the unit cells are of $LiVPO_4F$-type (Z = 2, with centrosymmetric vanadium octahedra) and the blue-filled area corresponds to the range of compositions for which the unit cells are of $LiVPO_4O$-type (Z = 4, with distorted vanadium octahedra). The Vegard's law is given for each parameter as a line.

Figure 3: Rietveld refinement of the structure of LVPF-25% (i.e. $LiVPO_4F_{0.45}O_{0.55}$) based on the combined analysis of Synchrotron X-ray (a) and Neutron (b) diffraction patterns. The observed intensities are plotted as red points, the theoretical Bragg positions are plotted as purple marks for the main phase and as grey ones for the secondary phase (i.e. $Li_3V_2(PO_4)_3$), the calculated intensities and the difference between observed and calculated intensities are plotted as black lines.

Figure 4: Structure of $LiVPO_4F_{1-y}O_y$ described in the LVPF-type unit cell (in the *P-1* space group): VO_4X_2 (X = O, F) octahedra in blue, PO_4 tetrahedra in pink and Lithium in purple.

Figure 5: Diffuse reflectance infrared spectra of $LiVPO_4O$ (grey line), $LiVPO_4F_{0.25}O_{0.75}$ (LVPF-5%, blue line), $LiVPO_4F_{0.45}O_{0.55}$ (LVPF-25%, purple line), $LiVPO_4F_{0.65}O_{0.35}$ (LVPF-50%, red line) and $LiVPO_4F$ (black line).

Figure 6: (a) V K-edge XANES spectra of the whole series of $LiVPO_4F_{1-y}O_y$ compounds with the enlargement of the pre-edge region in inset, showing the gradual growth of the vanadyl-type environment. (b) Evolution of the edge position and pre-edge integrated intensity as a function of the average oxidation of vanadium

Figure 7: Schematic view of the VO_4X_2 octahedra as a function of F substitution. The bond lengths are obtained by fitting the Fourier transforms of the k^2-weighted V K-edge EXAFS oscillations. The meaning of (i), (ii) and (iii) and the values of the corresponding probabilities (p_i, p_{ii}, p_{iii}) are specified in the text.

Figure 8: Galvanostatic profiles obtained versus Lithium at a C/10 rate for $LiVPO_4F_{0.25}O_{0.75}$ (LVPF-5%, blue line), $LiVPO_4F_{0.45}O_{0.55}$ (LVPF-25%, purple line) and $LiVPO_4F_{0.65}O_{0.35}$ (LVPF-50%, red line): (a) in the high voltage domain (i.e. between 3.0 and 4.6 V *vs* Li^+/Li) and (b) in the low voltage domain (i.e. between 3.0 and 1.0 V *vs* Li^+/Li). The derivative curves of their first cycle are given in inset.

Figure 9: Evolution of the discharge capacity of the $Li//LiVPO_4F_{1-y}O_y$ cells at different C-rates (from C/10 to 2C) as a function of the cycle number.

Table 1

		$LiVPO_4O$	LVPF-5%	LVPF-25%	LVPF-50%	$LiVPO_4F$
Cell parameters, *P-1*						
***a* (Å) =**		6.7320(1)	5.1568(2)	5.1626(1)	5.1651(1)	5.1689(1)
***b* (Å) =**		7.1942(1)	5.2871(2)	5.2946(1)	5.2995(1)	5.3087(1)
***c* (Å) =**		7.9204(1)	7.1722(2)	7.1899(2)	7.2147(1)	7.2621(1)
***α* (°) =**		89.843(1)	107.145(2)	107.224(1)	107.357(1)	107.591(1)
***β* (°) =**		91.272(1)	107.578(2)	107.608(2)	107.801(1)	107.973(1)
***γ* (°) =**		116.886(3)	98.611(2)	98.664(1)	98.499(1)	98.394(1)
V/Z ($Å^3$) =		85.510(9)	85.952(9)	86.286(6)	86.576(3)	87.141(6)
Z=		4	2	2	2	2
Estimated compositions (Vegard's law)		$LiVPO_4O$	$LiVPO_4F_{0.27}O_{0.73}$	$LiVPO_4F_{0.48}O_{0.52}$	$LiVPO_4F_{0.65}O_{0.35}$	$LiVPO_4F$
Chemical composition						
Molar ratios	**Li/V**	1.05(5)	0.98(5)	1.02(5)	1.01(5)	1.02(5)
	V/P	0.97(5)	1.04(5)	1.02(5)	1.04(5)	1.02(5)
C (wt. %)		/	2.58	5.95	7.06	5.97
F (wt. % / mol. %)		/	0.52 / 0.29	0.90 / 0.51	1.35 / 0.77	1.57 / 0.90
Estimated compositions (ICP-TGA)		$Li_{1.02}V_{0.97}PO_4O$	$Li_{1.02}V_{1.04}PO_4F_{0.29}O_{0.71}$	$Li_{1.02}V_{1.02}PO_4F_{0.51}O_{0.49}$	$Li_{1.05}V_{1.04}PO_4F_{0.77}O_{0.23}$	$Li_{1.04}V_{1.02}PO_4F_{0.90}O_{0.10}$
Magnetic properties						
χ_m T (emu/mol)		0.339 (ref. 2)	0.498	0.624	0.752	0.974 (ref. 2)
Average oxidation state of V^{n+}		4	3.75	3.55	3.35	3
Estimated compositions (Curie Weiss' law)		$LiVPO_4O$	$LiVPO_4F_{0.25}O_{0.75}$	$LiVPO_4F_{0.45}O_{0.55}$	$LiVPO_4F_{0.65}O_{0.35}$	$LiVPO_4F$

Table 2

	$LiVPO_4F_{0.65}O_{0.35}$ LVPF-50%		$LiVPO_4F_{0.45}O_{0.55}$ LVPF-25%		$LiVPO_4F_{0.25}O_{0.75}$ LVPF-5%	
Coordination	V(1)	V(2)	V(1)	V(2)	V(1)	V(2)
O(1) (x2)	/	1.936(8)	/	1.945(9)	/	1.920(9)
O(2) (x2)	/	1.997(6)	/	1.988(6)	/	2.012(9)
O(3) (x2)	1.991(6)	/	2.004(6)	/	1.985(9)	/
O(4) (x2)	1.964(6)	/	1.975(6)	/	1.988(9)	/
O(5)/F(1) (x2)	1.972(9)	1.929(7)	1.934(9)	1.945(9)	1.937(9)	1.922(9)
Average	1.976(7)	1.954(7)	1.971(7)	1.959(8)	1.972(9)	1.952(9)
Δ	6.5×10^{-5}	4.8×10^{-4}	5.3×10^{-5}	5.2×10^{-4}	2.8×10^{-4}	9.4×10^{-4}
BVS	3.13(1)	3.33(1)	3.15(1)	3.35(1)	3.22(1)	3.39(1)

Figure 1

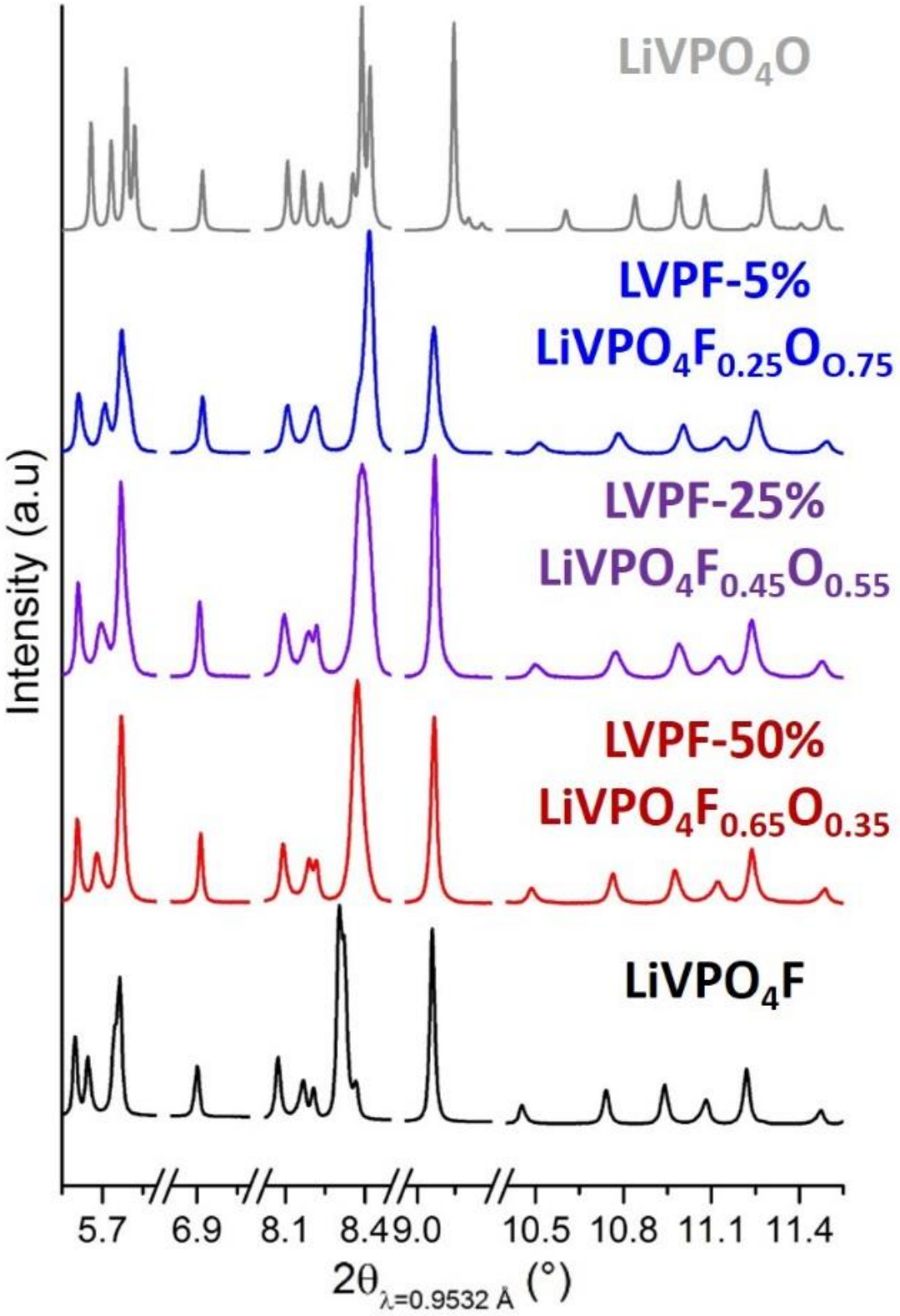
LiVPO4O
LVPF-5%
LiVPO4F0.25O0.75
LVPF-25%
LiVPO4F0.45O0.55
LVPF-50%
LiVPO4F0.65O0.35
LiVPO4F
Intensity (a.u)
5.7
6.9
8.1
8.4
9.0
10.5
10.8
11.1
11.4
2θλ=0.9532 Å (°)

Figure 2

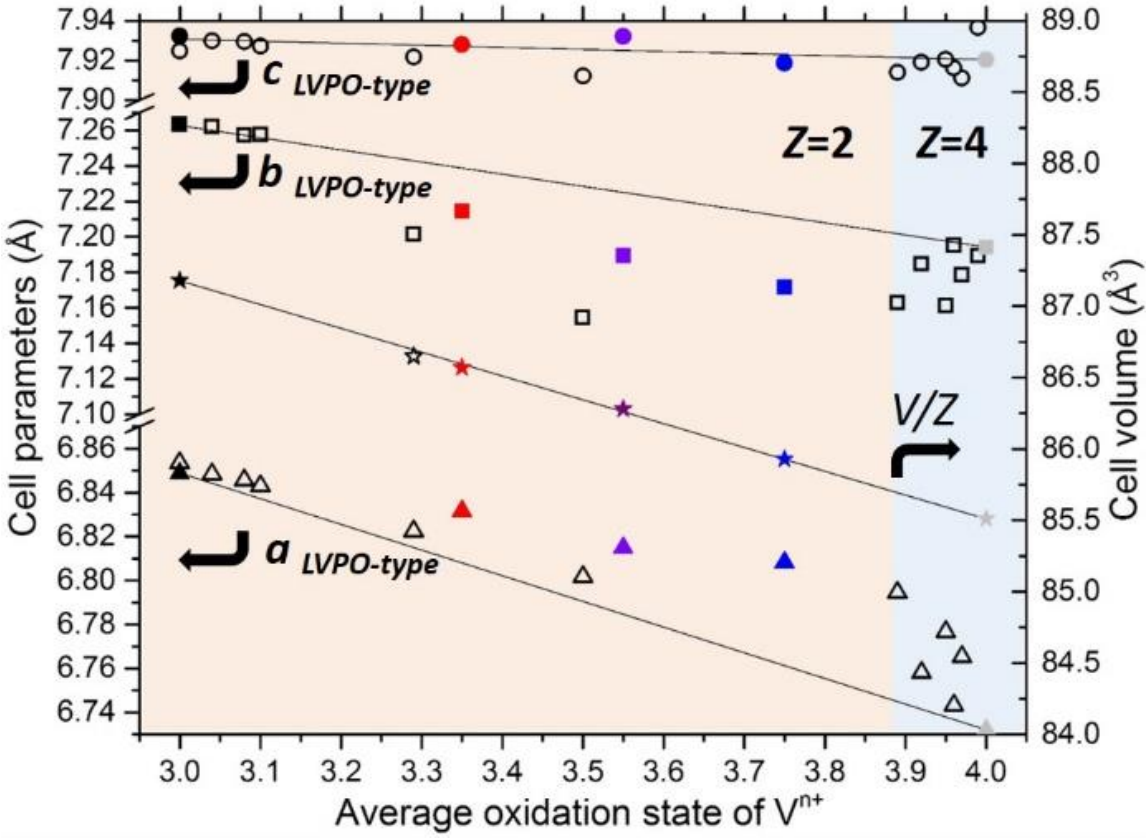
c LVPO-type
b LVPO-type
a LVPO-type
Z=2
Z=4
V/Z
Cell parameters (Å)
Cell volume (Å³)
Average oxidation state of V^n+
7.94
7.92
7.90
7.26
7.24
7.22
7.20
7.18
7.16
7.14
7.12
7.10
6.86
6.84
6.82
6.80
6.78
6.76
6.74
89.0
88.5
88.0
87.5
87.0
86.5
86.0
85.5
85.0
84.5
84.0
3.0
3.1
3.2
3.3
3.4
3.5
3.6
3.7
3.8
3.9
4.0

Figure 3

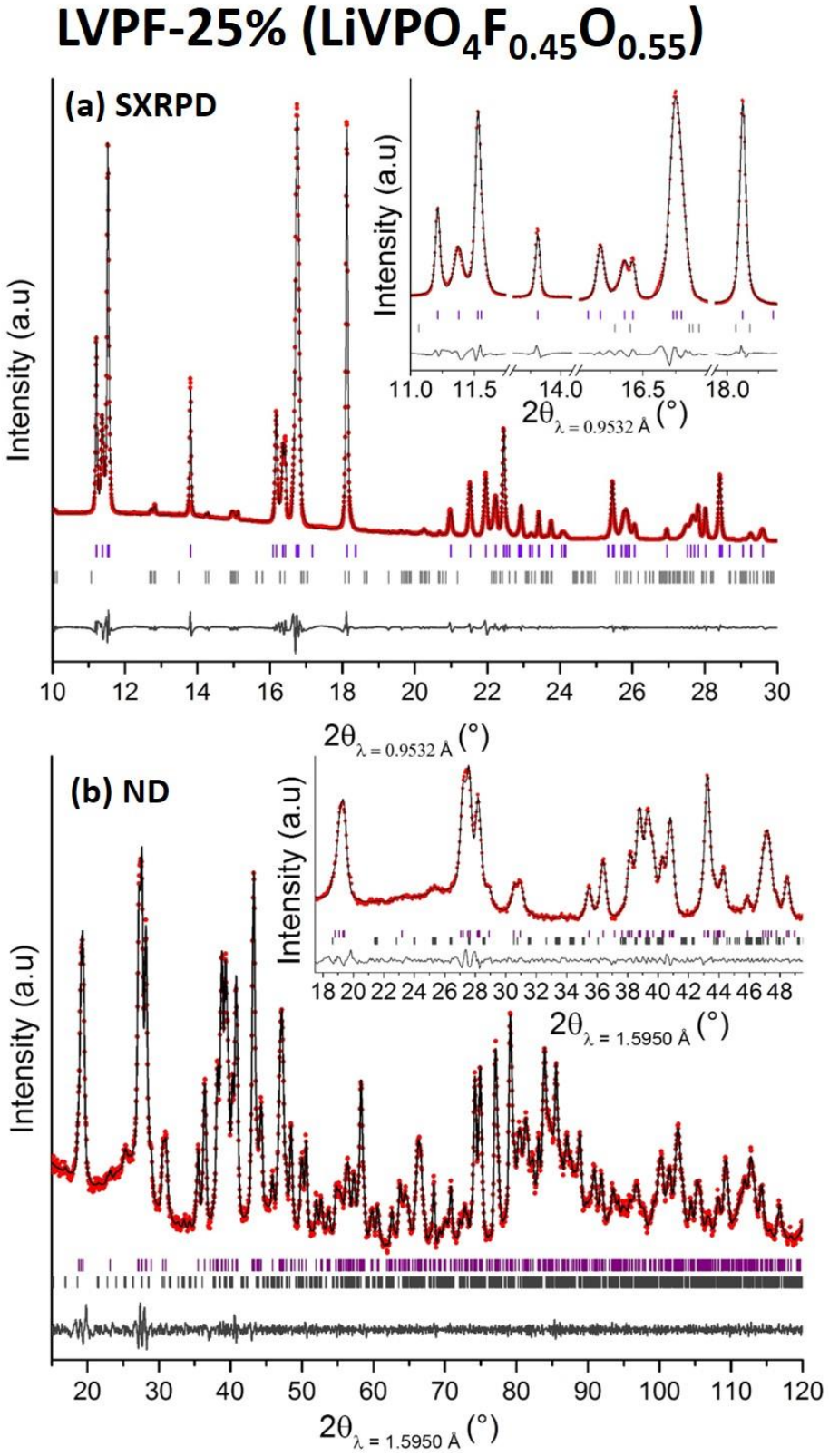
LVPF-25% (LiVPO4F0.45O0.55)
(a) SXRPD
Intensity (a.u)
2θλ = 0.9532 Å (°)
(b) ND
Intensity (a.u)
2θλ = 1.5950 Å (°)

Figure 4

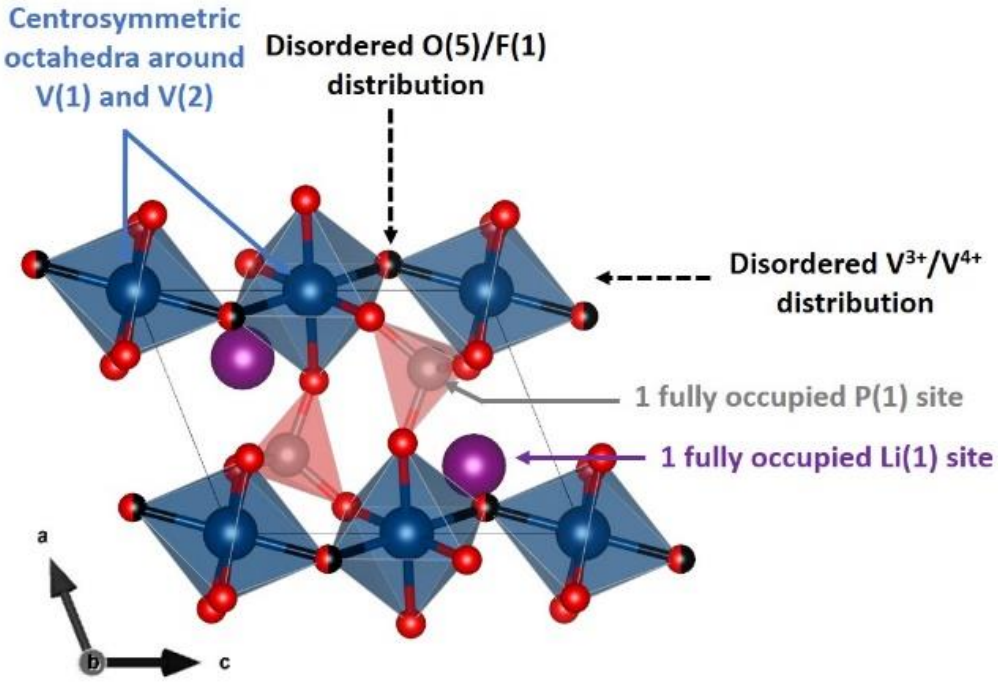
Centrosymmetric octahedra around V(1) and V(2)
Disordered O(5)/F(1) distribution
Disordered V^{3+}/V^{4+} distribution
1 fully occupied P(1) site
1 fully occupied Li(1) site
a
b
c

Figure 5

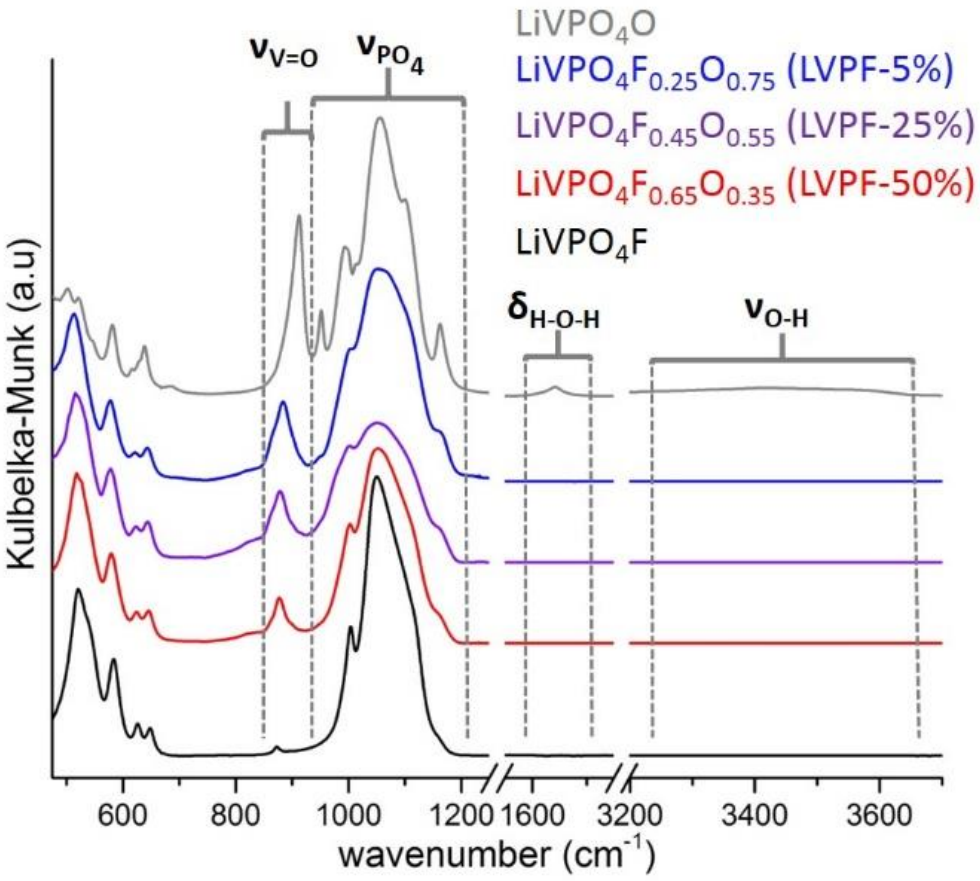
LiVPO4O
LiVPO4F0.25O0.75 (LVPF-5%)
LiVPO4F0.45O0.55 (LVPF-25%)
LiVPO4F0.65O0.35 (LVPF-50%)
LiVPO4F
νV=O
νPO4
δH-O-H
νO-H
Kulbelka-Munk (a.u)
600
800
1000
1200
1600
3200
3400
3600
wavenumber (cm-1)

Figure 6

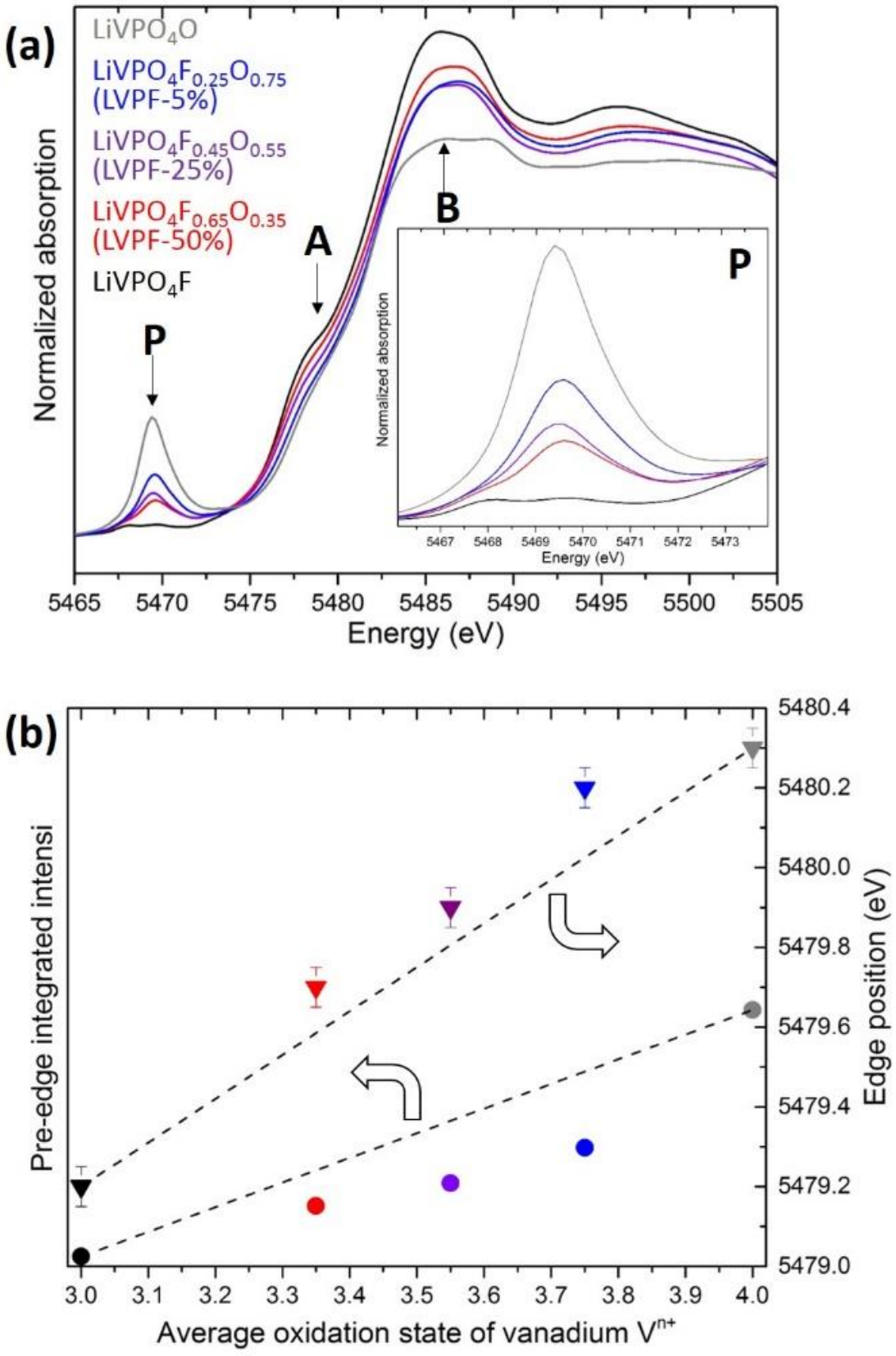
(a)
LiVPO4O
LiVPO4F0.25O0.75
(LVPF-5%)
LiVPO4F0.45O0.55
(LVPF-25%)
LiVPO4F0.65O0.35
(LVPF-50%)
LiVPO4F
P
A
B
Normalized absorption
Energy (eV)
5465
5470
5475
5480
5485
5490
5495
5500
5505
5467
5468
5469
5470
5471
5472
5473
(b)
Pre-edge integrated intensi
Edge position (eV)
Average oxidation state of vanadium V^n+
3.0
3.1
3.2
3.3
3.4
3.5
3.6
3.7
3.8
3.9
4.0
5479.0
5479.2
5479.4
5479.6
5479.8
5480.0
5480.2
5480.4

Figure 7

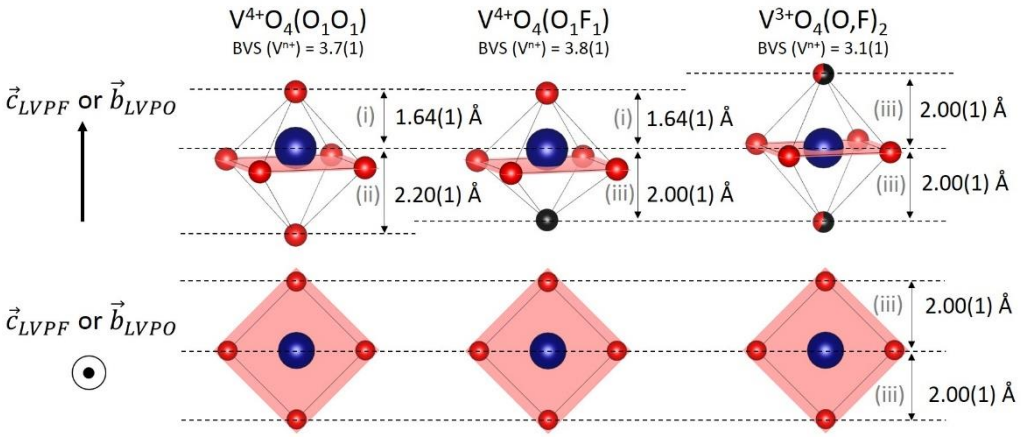

Probabilities	6*p_{ii} (%)	6*(p_i-p_{ii}) (%)	6*(1-p_i) (%)
$LiVPO_4F$	0	0	100
$LiVPO_4F_{0.65}O_{0.35}$ LVPF-50%	10	25	65
$LiVPO_4F_{0.45}O_{0.55}$ LVPF-25%	20	35	45
$LiVPO_4F_{0.25}O_{0.75}$ LVPF-5%	45	30	25
$LiVPO_4O$	100	0	0

Figure 8

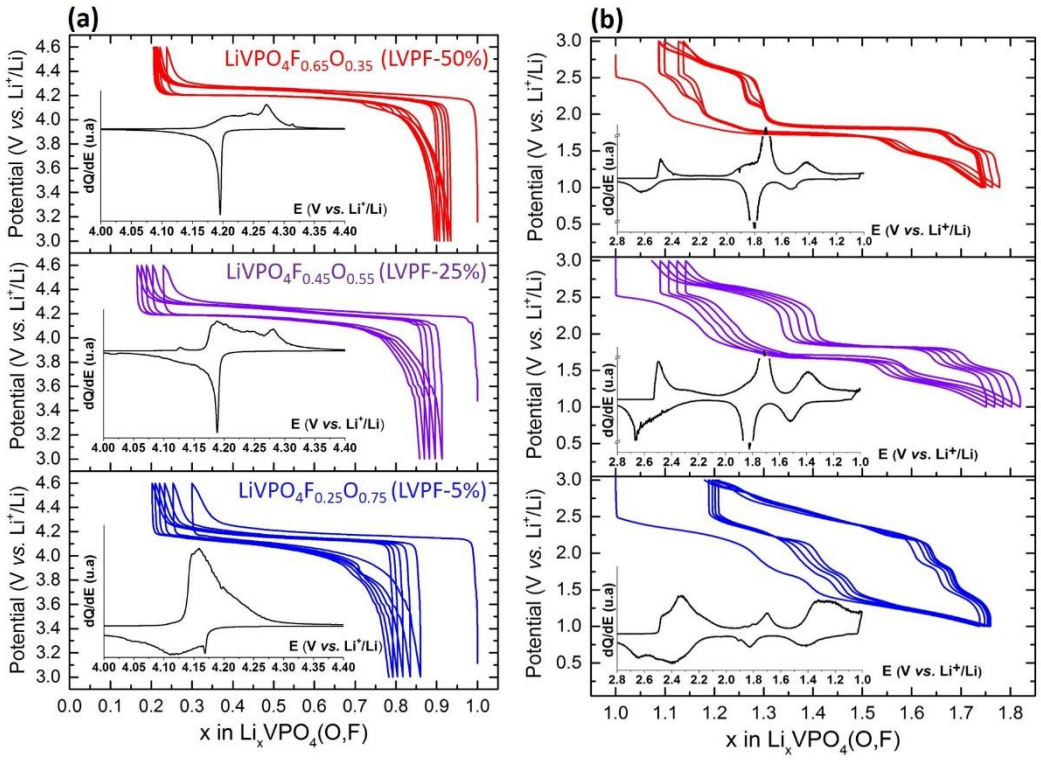
(a)
(b)
LiVPO4F0.65O0.35 (LVPF-50%)
LiVPO4F0.45O0.55 (LVPF-25%)
LiVPO4F0.25O0.75 (LVPF-5%)
Potential (V vs. Li+/Li)
dQ/dE (u.a)
E (V vs. Li+/Li)
x in LixVPO4(O,F)

Figure 9

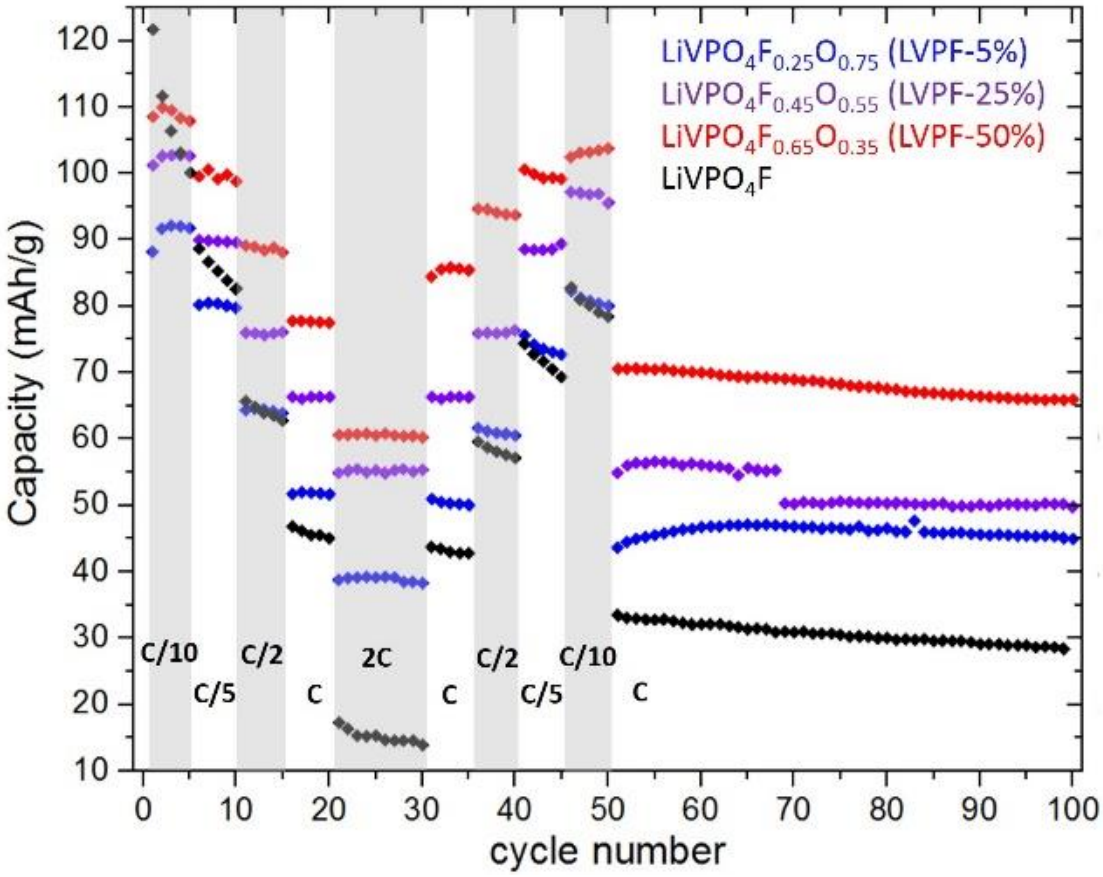
LiVPO4F0.25O0.75 (LVPF-5%)
LiVPO4F0.45O0.55 (LVPF-25%)
LiVPO4F0.65O0.35 (LVPF-50%)
LiVPO4F
Capacity (mAh/g)
cycle number
C/10
C/5
C/2
C
2C
C
C/2
C/5
C/10
C